



Evidence of fluid evolution of Baoshan Cu–Pb–Zn polymetallic deposit: Constraints from in-situ sulfur isotope and trace element compositions of pyrite

Jun-ke ZHANG^{1,2}, Yong-jun SHAO^{1,2}, Ke CHEN^{1,2}, Hua-jie TAN^{1,2},
Rui-chang TAN^{1,2}, Tian-dong ZHANG^{1,2}, Zhong-fa LIU^{1,2}

1. Key Laboratory of Metallogenic Prediction of Nonferrous Metals, Ministry of Education, Central South University, Changsha 410083, China;
2. School of Geosciences and Info-Physics, Central South University, Changsha 410083, China

Received 29 September 2021; accepted 17 November 2021

Abstract: In-situ LA-ICP-MS and S isotopes of pyrite from the Baoshan Cu polymetallic deposit were conducted to investigate the ore-forming process and the enrichment mechanism of elements. Three generations of pyrite (Py I, Py II, and Py III) in the skarn-type ores and pyrite in the carbonate-hosted sulfide ores from central, western, and northern (C_Py, W_Py, and N_Py) mining districts are selected for comparison. Compared with Py I and Py III, the contents of most elements in Py II are apparently higher. The As and Se contents are high within a wide range and are decoupled in the growth band of the C_Py. The highest As, Se, and Pb contents were found in W_Py and N_Py. These results indicate the drastic changes in the temperature and fluid mixing during the mineralization. The occurrence of fluctuation and change in temperature and $f(O_2)$ was triggered by intermittent pulses of magmatic-hydrothermal fluids, mixing with meteoric water, and water–rock interactions. The sulfur isotopes of all species of pyrite indicated the magmatic source. The change in the $f(O_2)$ conditions caused slight differences in the sulfur isotope compositions. Consequently, a metallogenic model was proposed to explain the ore-forming processes.

Key words: pyrite; trace element; in-situ S isotope; hydraulic fracturing; fluid mixing

1 Introduction

Intense and complex tectonic movement and the associated magmatism have resulted in the South China Block being enriched in abundant mineral resources [1–5]. The Qin-hang and Nanling ore belts are typical Cu–Pb–Zn and W–Sn polymetallic mineralization belts in the South China district, respectively [6–9]. These two metallogenic belts overlap in the southern part of Hunan Province, where the Cu–Pb–Zn and W–Sn deposits are spatially and temporally coupled [1]. Compared to the well-documented causative magmas of the Cu–Pb–Zn and W–Sn polymetallic mineralization,

the details of the ore-forming process and the enrichment mechanism of metallogenic elements have not yet been thoroughly investigated, which severely limits our understanding of the coupling of Cu–Pb–Zn and W–Sn mineralization [10–13].

The Baoshan Cu–Pb–Zn polymetallic deposit, as a representative Cu polymetallic deposit in the overlap zone of these two mineralization belts, has attracted extensive attention and is considered to be an ideal area for studying Cu polymetallic mineralization [14–16]. Previous studies have accumulated a large amount of data and examined the ore-forming granodiorite porphyry in detail [10,11,17]. However, the ore-forming process and enrichment mechanism of the metallogenic

elements of the Cu polymetallic mineralization in this region lack solid constraints [16,18–20]. Therefore, it was necessary to conduct detailed geochemical and isotopic analyses of the Baoshan deposit in order to gain a better understanding of the element enrichment mechanism and ore-forming processes of the metallogenic Cu–Pb–Zn system in this region.

In the Baoshan deposit, the Cu primarily occurs in the skarn-type ores, whereas Pb–Zn–Ag is related to the hydrothermal vein-type ores hosted by the carbonates [6,16,21]. The understanding of the whole mineralization process and conditions is limited due to the significant differences in mineralization types and lacking a common mineral. Thus, pyrite, which is widespread in both the skarn-type ores and hydrothermal vein-type ores, was selected for comparison. In this study, In-situ LA-ICP-MS trace element and S isotope analyses were performed on pyrite from the Baoshan Cu–Pb–Zn polymetallic deposit. Based on these previous fluid inclusion research and trace element geochemistry for pyrite, geochemical constraints on the ore-forming process and enrichment mechanism

of the metallogenic elements in the Baoshan deposit are given, which can provide evidence of the coupling of the Cu–Pb–Zn and W–Sn mineralization in this region.

2 Geological setting

2.1 Regional geology

The Baoshan Cu–Pb–Zn polymetallic deposit is located near the amalgamation of the Yangtze and Cathaysia blocks (Fig. 1) [22–25], where the abundant polymetallic mineralization was generated in four dominant episodes (the Silurian, Triassic, Jurassic and the Cretaceous) and is associated with multi-stage magmatism (Fig. 1) [26–29]. Some of the deposits are associated with the Nanling ore belt and are enriched in Sn(–W) (e.g., the Xianghualing, Huangshaping, Shizhuyuan, and Furong deposits), while the others are associated with the Qin-hang ore belt and are enriched in Cu (e.g., the Baoshan and Hehuaping deposits) [6].

In the South Hunan district, the regional metamorphosed basement comprised pre-Silurian strata that were intensely metamorphosed and

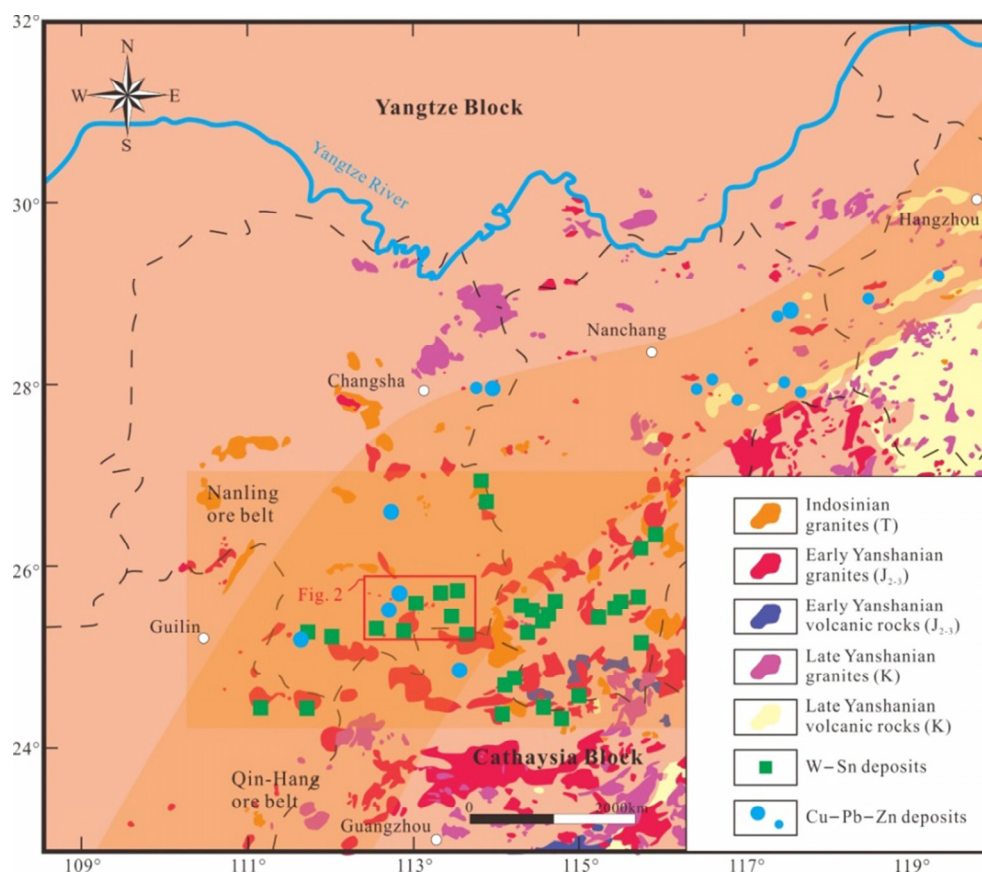


Fig. 1 Simplified regional geological map showing distributions of Jurassic granites and W–Sn and Cu–Pb–Zn deposits in South China Block (Modified from Refs. [6,30])

deformed during the Caledonian orogeny. Devonian–Triassic limestone and shale, in which NNE- and NE-trending faults and folds were widely developed during the Indosinian orogeny and the subduction of the Paleo-Pacific Plate during the Triassic–Cretaceous, unconformably overlie the basement rocks (Fig. 2) [13,23,25,27]. Jurassic granitoids are widely distributed and are accompanied by a series of Cu and Sn(–W) polymetallic deposits in this region (Fig. 2).

2.2 Deposit geology

The Baoshan deposit is a representative Cu–Pb–Zn polymetallic deposit, containing Cu–Mo skarn mineralization in the central mining district and Pb–Zn hydrothermal-vein mineralization in the eastern, western, and northern mining districts (Fig. 3). The sedimentary strata primarily include the Upper Devonian Xikuangshan Formation; the Lower Carboniferous Menggong’ao, Shidengzi, Ceshui, and Zimenqiao Formations; and the Middle-Upper Carboniferous Hutian Group. The Cu skarn is hosted in the limestone of the Shidengzi Formation and is controlled by the NE-trending Baoling inversion anticline; while the Pb–Zn hydrothermal vein-type mineralization primarily occurs in the dolomite of the Zimenqiao Formation along the faults (e.g., F₂₁, Fig. 4). As a

typical skarn deposit [32], breccia and fluid escape structures are widely developed in the Baoshan deposit (Figs. 5(a–c)), especially near the faults. In addition, Fe–Mn oxides are normally observed on the surface (Fig. 5(d)). The granodiorite porphyry is a possible causative pluton and was formed at 162–155 Ma [11,15,17,31,33,34]. It has a porphyritic or porphyritic-like texture. It is primarily composed of plagioclase, K-feldspar, biotite, and quartz with the mafic microgranular enclave [34]. Molybdenite Re–Os age of (160±2) Ma [15], pyrite Rb–Sr isochron of (174±7) Ma [20], and grossular-rich garnet U–Pb dating of (162.6±2.9) Ma [31] constrain the ore-forming age of the Baoshan deposit.

3 Sampling and analytical methods

A total of 5 representative samples were collected for trace element and in-situ sulfur isotope analyses. Two samples were collected from a skarn orebody in the central mining district (451-1 and 451-3). Three carbonate-hosted ores were collected from the central (801-10), western (724-6), and northern (729-2) mining districts. A detailed description of the sampling locations, textures, and mineral assemblages are presented in Table 1.

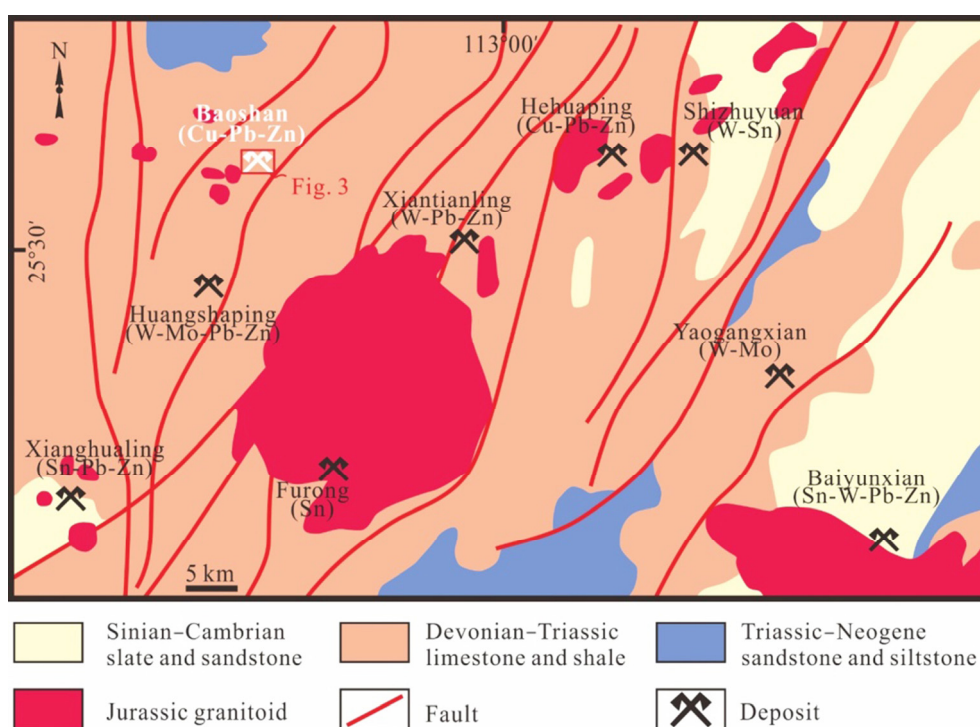


Fig. 2 Sketch map of secondary regional geology showing tectonics and distribution of mineral resources [31]

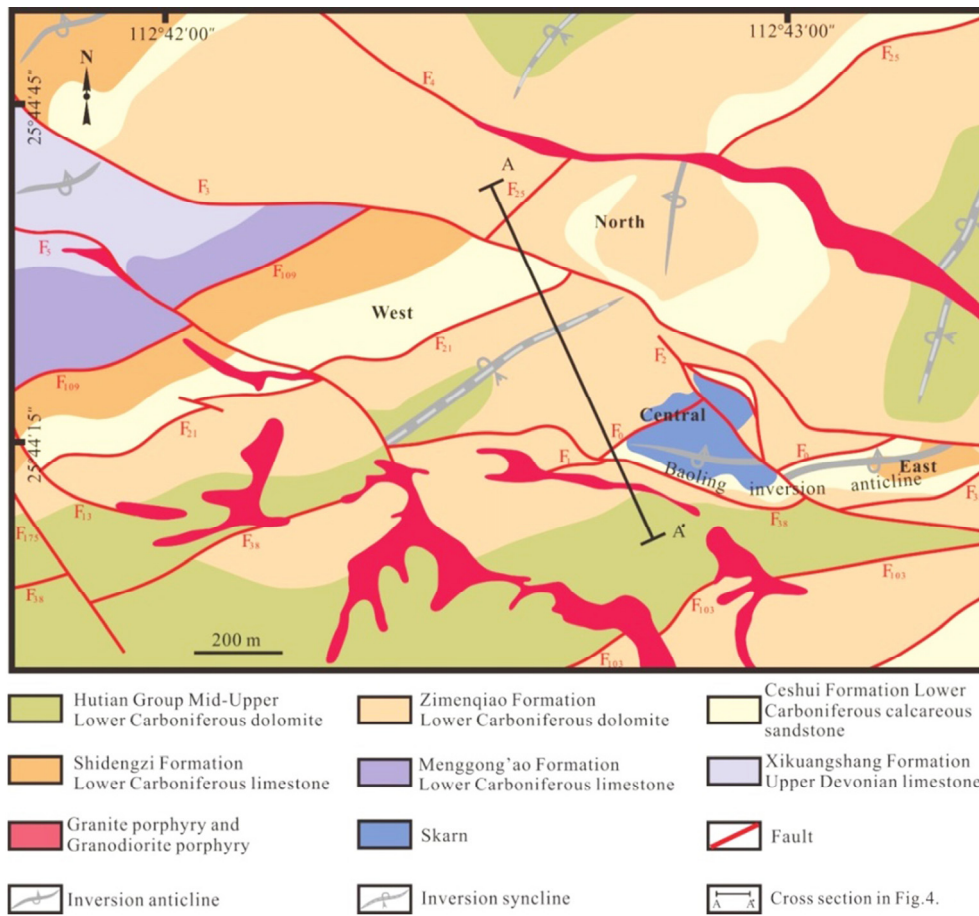


Fig. 3 Simplified geologic map of Baoshan deposit (Modified from Ref. [21])

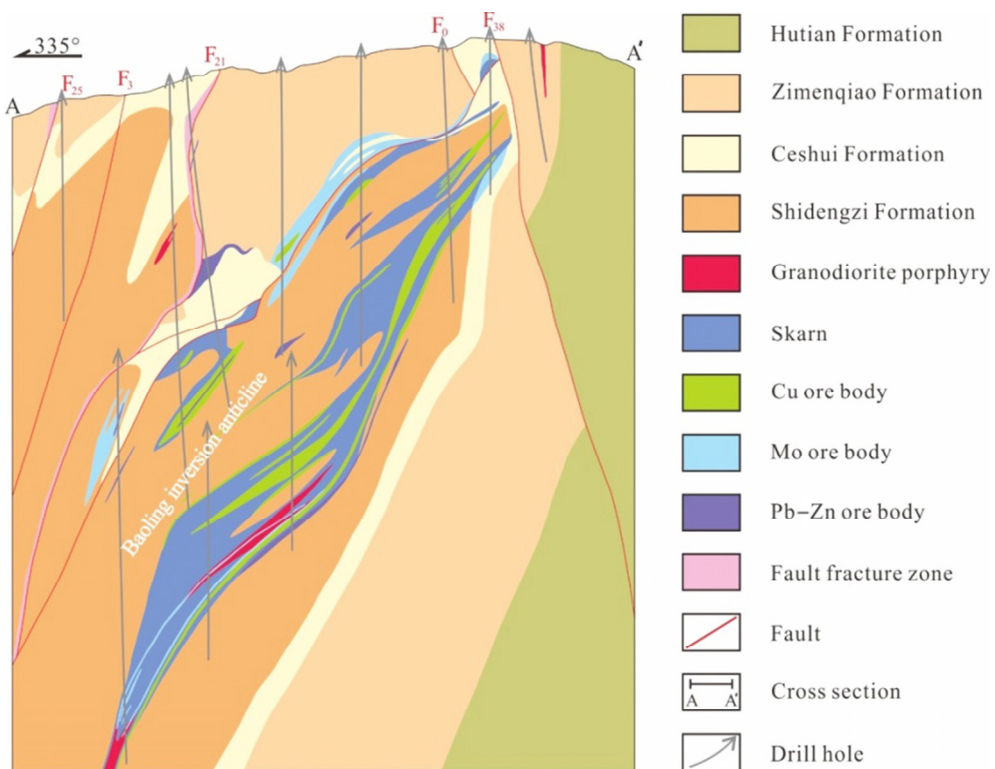


Fig. 4 Geological cross section of line 169 through Baoshan deposit (Modified from Ref. [6])

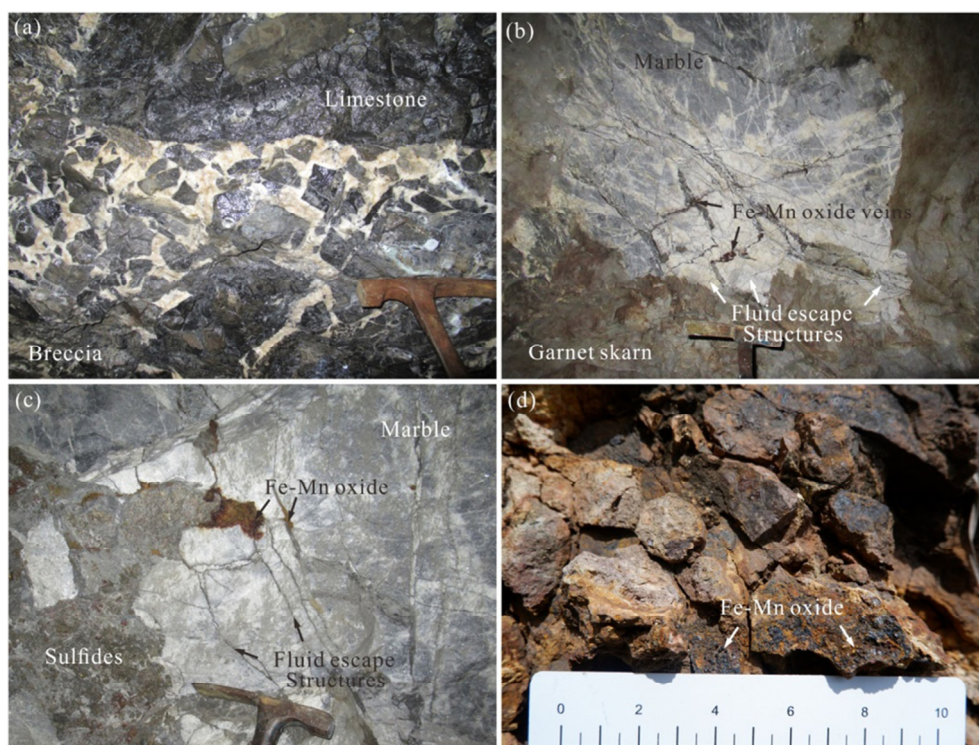


Fig. 5 Breccia and fluid escape structures in Baoshan deposit: (a) Limestone breccia cemented by carbonate minerals; (b) Hydrothermal fluids escaped from skarn into marble accompanied by Fe–Mn oxide veins; (c) Ore-forming fluid escaped into distal marble; (d) Fe–Mn oxides widely formed when hydrothermal fluids reaching surface

Table 1 Locations and mineral features of studied samples in Baoshan Cu–Pb–Zn deposit

Sample	No.	Location	Mining district	Mineral assemblage
Skarn-type	451-1	Southwest 50 m; south of line 165	Central	Mag+Ccp+Py+Qtz+Cb
	451-3	Southwest 50 m; south of line 165	Central	Grt+Di+Ccp+Py+Ttr+Mag+Hem+Qtz+Cb
	801-10	Southwest –190 m level; stope 159	Central	Ccp+Py+Sp+Gn+Fl+Qtz
Hydrothermal Vein-type	724-6	Northwest –110 m level; between line 159 and 161; F21	Western	Py+Sp+Gn+Qtz±Cb
	729-2	North –110 m level; north of line 177; F25	Northern	Asp+Py+Sp+Gn+Qtz+Cb

Mag: Magnetite; Ccp: Chalcopyrite; Py: Pyrite; Qtz: Quartz; Cb: Carbonates; Grt: Garnet; Di: Diopside; Ttr: Tetrahedrite; Hem: Hematite; Sp: Sphalerite; Gn: Galena; Fl: Fluorite

3.1 LA-ICP-MS analysis

Standard polished thin sections (~30 μm) were prepared for ore microscopy and analysis of the trace elements via LA-ICP-MS. The trace element analyses of the 5 samples were performed using the LA-ICP-MS system at Guangzhou Tuoyan Testing Technology Co., Ltd. (China), consisting of a 193 nm New Wave Research Excimer laser and an Agilent 7500i quadrupole ICP-MS. This laser ablation system included a wire signal smoothing device. The beam spot size, laser energy, and frequency were 40 μm, 5 J/cm², and 6 Hz,

respectively. Helium was used as the carrier gas of the ablated materials. Standards NIST 610, GSE-2G, and MASS-1 were used to calibrate the single mineral trace element contents. Each LA-ICP-MS analysis was composed of 50 s of background measurement and 40 s of sample measurement. The offline processing of the original data was completed using iolite.

3.2 In-situ sulfur isotope analysis

The δ³⁴S compositions of the pyrite and associated sphalerite were measured in-situ using a

RESOLUTION SE laser-ablation system attached to a Thermo Fisher Scientific Neptune Plus MC-ICP-MS at the Beijing Createch Testing Technology Co., Ltd. (China). In order to eliminate surface contamination, each spot was pre-ablated before analysis. The spot size, frequency, and laser energy were 35 μm , 8 Hz, and 8 J/cm^2 , respectively. Helium (~ 150 mL/min) was used as the carrier gas. The S isotope data were acquired via static multi-collection in high-resolution mode with 27 s of each spot for integration. The Neptune multicollector inductively coupled plasma mass spectrometer (MC-ICP-MS) was tuned before the laser analyses using a standard (balmat FeS, MXG, and balmat ZnS) to obtain the maximum sensitivity. The sample-standard bracketing method was used to calibrate the instrumental mass discrimination.

3.3 Principle component analysis

Principle component analysis (PCA) is an unsupervised classification method that is widely used in the field of geochemical exploration. It can highlight the significant features among variables, reveal the underlying correlations between individuals, and reduce the dimensions of a dataset to project the data in two dimensions for visualization. The data preprocessing method used is consistent with that used by FRENZEL et al [35]. Therefore, Mn, Co, Ni, Cu, Zn, As, Se, Mo, Ag, Sb, Te, Au, Tl, and Pb were selected for the PCA. The calculation part of the PCA was conducted using the scikit-learn package in Python language [36].

4 Results

4.1 Paragenesis and microstructure of pyrite

The skarn-hosted pyrite was classified into three generations (Py I, Py II, and Py III) based on the petrology, metasomatic relationship, and mineral assemblage. The Py II and Py III appeared as a vein cutting the skarn (Fig. 6(a)). Py I is predominantly present in the skarn ores, with a coarse-grained subhedral cubic to allotriomorphic texture and relatively smooth surfaces (Fig. 6(b)). It usually exhibits brittle deformation characteristics with networked cracks and is generally replaced by carbonate veins or later sulfides (e.g., magnetite; Fig. 6(c)). Py II has a typical colloform structure with concentric or rhythmic bands (Figs. 6(c–e)). It coexists with chalcopyrite, magnetite, and quartz

and can also be observed coexisting with skarn minerals. The magnetite precipitated earlier than the Py II and was replaced by the latter resulting in an isolated granular texture (Fig. 6(d)). Py III is fine-grained with an anhedral texture. It occurs as veinlets and growths along the cracks or edges of the Py II and chalcopyrite (Fig. 6(e)).

The hydrothermal vein-type pyrite is predominantly found in the carbonates in the western and northern mining districts, without any accompanied skarn minerals, and it is generally associated with sphalerite, galena, sulfosalt minerals (e.g., bournonite), fluorite, carbonate, and minor quartz. This type of pyrite can be easily distinguished from the skarn-hosted pyrite (Figs. 6(f–k)). The microstructures and trace element compositions of this type of pyrite are significantly different among different mining districts. This type of pyrite is coarse-grained with a euhedral to subhedral texture in the central mining district (C_Py, Fig. 6(f)). An oscillating band was observed in C_Py after NaClO-etching (Fig. 6(g)), indicating a relatively slow crystallization process and intermittent pulses of ore-forming fluids. The coexisting minerals are primarily In-rich sphalerite [21], galena, quartz, and fluorite. In the western mining district, the vein-type pyrite is coarse-grained with a subhedral to the anhedral texture (W_Py, Fig. 6(i)). No distinct compositional or structural zonation was observed after NaClO-etching. In the northern mining district, this type of pyrite exhibits a core-mantle-rim texture (Fig. 6(k)).

4.2 In-situ LA-ICP-MS trace element data

A total of 60 LA-ICP-MS spot analyses were completed on pyrite, including 10 spots on each type (Fig. 7 and Table 2). Significant differences were found in the trace element compositions of the different types of pyrite. The contents of most of the elements (e.g., Mn, Co, Ni, Cu, In, and Sn) exhibit a mutation relationship between Py I and Py II, whereas they exhibit a gradient or evolution relationship between Py II and Py III. Py II has the highest Ag (71 ppm) and Tl (139 ppm) contents. In the Baoshan deposit, Ni and Bi can be used to effectively distinguish the skarn-hosted pyrite (Py I, Py II, and Py III) from the carbonate-hosted pyrite (C_Py, W_Py, and N_Py) since they are enriched in the former. In the central mining district, all of the

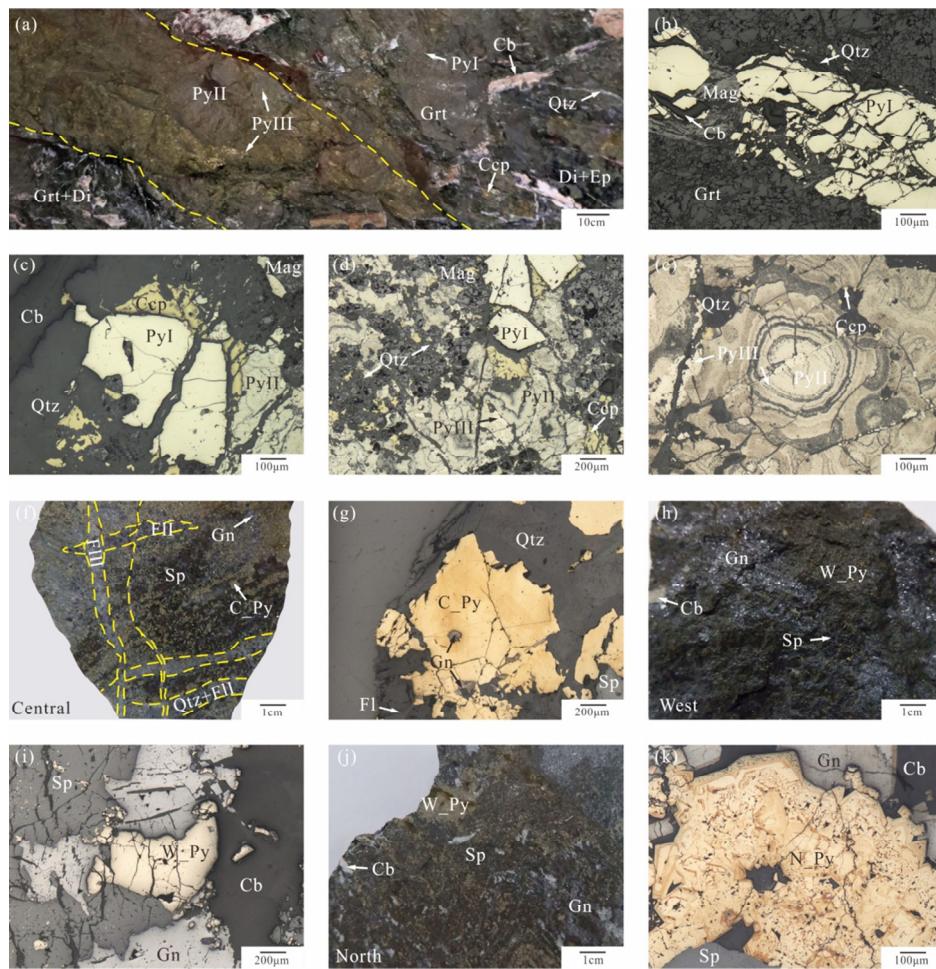


Fig. 6 Skarn-hosted (a–e) and carbonate-hosted (f–k) pyrite in Baoshan deposit: (a) Massive garnet (Grt)-diopside (Di) skarn with subhedral pyrite (Py I) cut by pyrite (Py II and Py III) vein; (b) Py I with crushed texture, replaced by magnetite (Mag) in skarn; (c) Py I replaced by magnetite; (d) Magnetite replaced by colloform pyrite (Py II) with an island appearance; (e) Colloform pyrite (Py II) cut by later pyrite veinlet (Py III); (f) Vein-type pyrite coexisting with sphalerite (Sp), galena (Gn), quartz (Qtz), and fluorite (Fl) in central mining district (C_Py); (g) Growth bands in C_Py after NaClO-etching; (h) Vein-type pyrite coexisting with sphalerite (Sp), galena (Gn), and carbonates (Cb) in western mining district (W_Py); (i) W_Py without compositional zonation after NaClO-etching, replaced by sphalerite and galena; (j) Vein-type pyrite coexisting with sphalerite (Sp), galena (Gn), and carbonates (Cb) in northern mining district (N_Py); (k) N_Py exhibiting core-mantle-edge structure after NaClO-etching

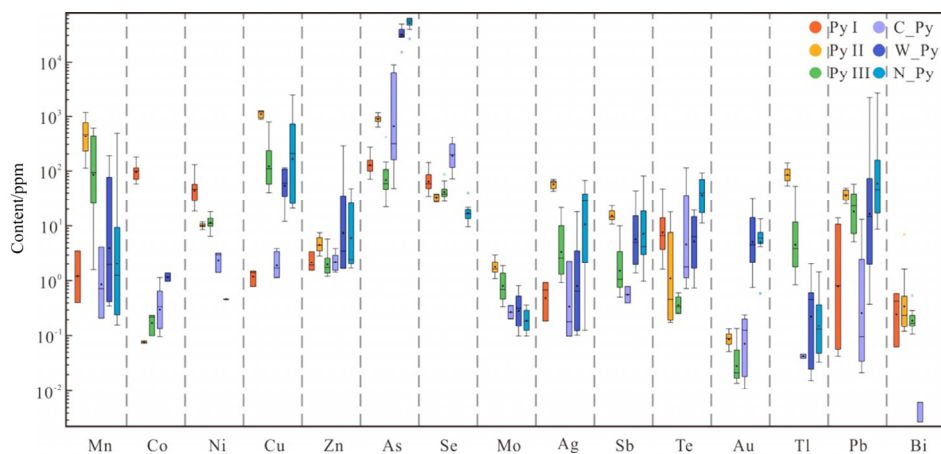


Fig. 7 Trace element contents of pyrite from Baoshan deposit, grouped into six main pyrite types (Py I, Py II, Py III, C_Py, W_Py, and N_Py)

Table 2 LA-ICP-MS results for different pyrite species (ppm)

Sample		Mn	Co	Ni	Cu	Zn	As	Se	Mo
Py I (N=10)	Avg	1.982	100.2	50.63	1.226	2.297	134.6	71.08	bdl
	Max	3.556	176.4	128.5	1.487	3.428	265.8	141	bdl
	Min	0.409	58.2	18.36	0.783	1.541	71.09	34.8	bdl
Py II (N=10)	Avg	537.5	0.076	10.16	1116	4.788	903.7	33.2	1.861
	Max	1186	0.08	11.79	1268	7.483	1169	38.05	3.002
	Min	111.1	0.073	8.531	888.8	2.878	641	26.74	1.085
Py III (N=10)	Avg	210.8	0.187	11.77	186.5	2.263	99.71	44.39	0.937
	Max	612.4	0.239	18.06	790.2	5.793	413.8	87.09	1.869
	Min	1.582	0.099	6.511	40.57	1.192	22.04	27.94	0.341
C_Py (N=10)	Avg	1.695	0.427	2.56	2.164	2.361	2620	213.2	0.282
	Max	4.158	1.139	3.24	3.915	3.923	8953	407.1	0.362
	Min	0.213	0.096	1.412	1.129	1.429	48.33	72.46	0.207
W_Py (N=10)	Avg	48.29	1.174	bdl	66.61	51.43	32428	bdl	0.361
	Max	186.8	1.376	bdl	113.3	280.3	47978	bdl	0.816
	Min	0.353	0.972	bdl	11.91	1.65	15223	bdl	0.098
N_Py (N=10)	Avg	72.4	bdl	bdl	500.1	13.57	51382	18.17	0.21
	Max	493.9	bdl	bdl	2452	47.7	61704	40.02	0.366
	Min	0.16	bdl	bdl	20.87	1.691	26017	9.571	0.098
Sample		Ag	Cd	Sb	Te	Au	Tl	Pb	Bi
Py I (N=10)	Avg	0.598	bdl	bdl	11.95	bdl	bdl	4.761	0.359
	Max	0.926	bdl	bdl	47.22	bdl	bdl	13.96	0.583
	Min	0.189	bdl	bdl	1.609	bdl	bdl	0.042	0.062
Py II (N=10)	Avg	58.47	1.261	15.57	4.334	0.088	88.83	37.03	1.033
	Max	70.76	1.789	23	17.8	0.132	138.7	49.12	7.02
	Min	43.27	0.988	10.77	0.178	0.051	53.72	25.08	0.12
Py III (N=10)	Avg	5.958	bdl	2.591	0.386	0.043	10.11	24.48	0.213
	Max	21.43	bdl	10.01	0.6	0.134	52.86	57.78	0.54
	Min	0.921	bdl	0.507	0.257	0.014	0.841	5.219	0.107
C_Py (N=10)	Avg	0.857	bdl	0.591	22.97	0.117	0.043	2.309	0.004
	Max	2.289	bdl	0.781	112.3	0.243	0.046	13.07	0.006
	Min	0.097	bdl	0.402	0.721	0.011	0.039	0.022	0.003
W_Py (N=10)	Avg	3.102	bdl	11.42	8.329	8.763	0.565	256.4	bdl
	Max	17.98	bdl	43.8	19.33	31.8	2.032	2192	bdl
	Min	0.102	bdl	1.378	0.731	0.751	0.015	0.379	bdl
N_Py (N=10)	Avg	26.28	bdl	16.33	45.71	6.241	0.316	320.5	bdl
	Max	67.84	bdl	81.74	92.53	13.33	1.436	2664	bdl
	Min	0.125	bdl	0.973	11.13	0.568	0.034	8.63	bdl

bdl: Below detective line

types of pyrite (Py I, Py II, Py III, or C_Py) are characterized by Se enrichment ((26–407) ppm). The W_Py and N_Py had the highest Au (up to 31 ppm) and As (up to 61703 ppm) contents, respectively.

4.3 In-situ sulfur isotope compositions of pyrites

The in-situ S isotope compositions of the pyrite from the Baoshan Cu–Pb–Zn polymetallic deposit are shown in Fig. 8 and Table 3. A total of 52 spots were measured, including 32 spots on the pyrite and 20 spots on the sphalerite that coexisted with the pyrite. The skarn-hosted pyrites (Py I, Py II, and Py III) have relatively low S isotope values and exhibit an increasing trend ((3.76–3.98)‰, (3.85–4.59)‰, and (4.03–4.62)‰, respectively). In comparison, the co-existing sphalerite has the highest S isotopic values (6.07–7.53)‰. The carbonate-hosted pyrites (C_Py, W_Py, and N_Py) have higher S isotopic values ((4.13–4.70)‰,

(1.85–5.74)‰, and (4.93–5.86)‰, respectively). The co-existing sphalerites (C_Sp, W_Sp, and N_Sp) have lower S isotopic values of (3.41–4.60)‰, (4.79–5.21)‰, and (4.78–5.23)‰, respectively.

4.4 Principal component analysis

PCA was conducted on the LA-ICP-MS data for the above types of pyrite (Fig. 9). The first two principal components account for 74.79% of the element content variability, indicating that the significant differences in the trace element compositions of the different types of pyrite can be effectively distinguished on the PC2 vs PC1 plane (Fig. 9(b)). First principal component (PC1) analysis accounts for 47.93% of the variance and is primarily a measure of the Cu, Ag, Sb, Tl, and Pb. PC2, which accounts for 26.86% of the variance, includes Mn, Se, Ni, Mo, and Tl, which have positive signs, and As, Te, and Au, which have

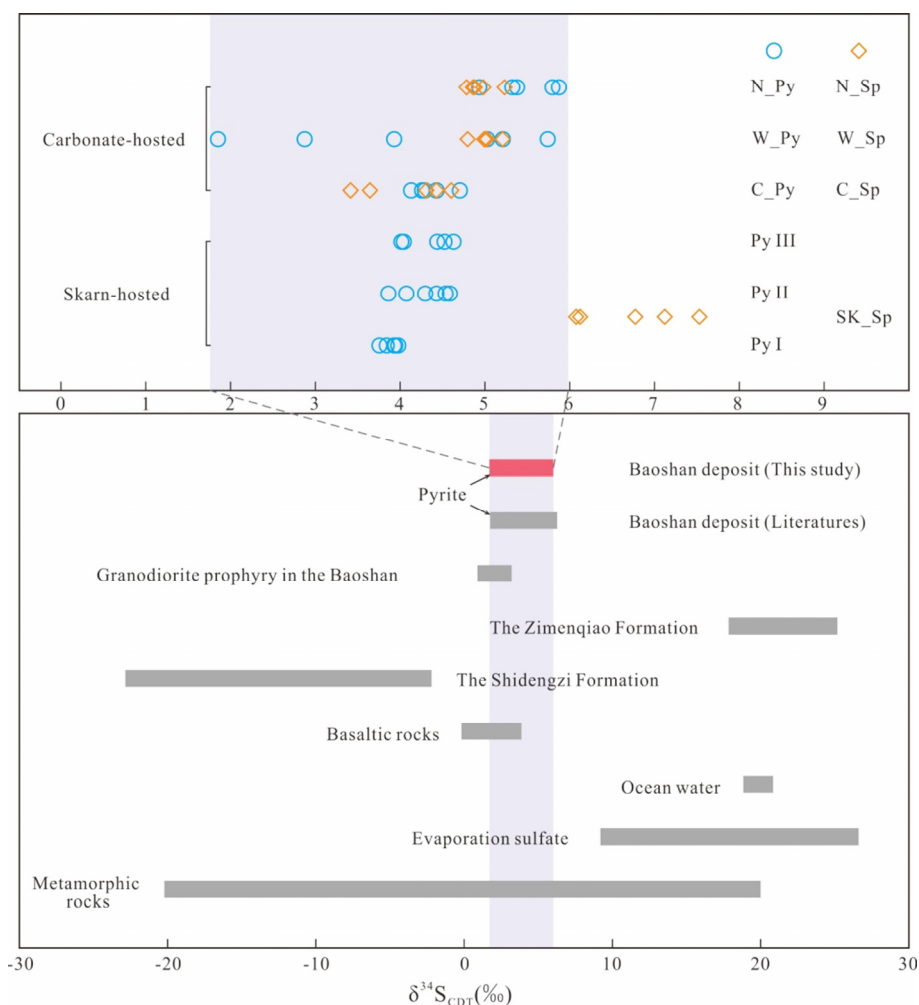


Fig. 8 $\delta^{34}\text{S}$ values of pyrite and sphalerite from Baoshan deposit ($\delta^{34}\text{S}$ values of other sulfides from the Baoshan deposit and those of related geological units from published data [6,18–20,37,38])

Table 3 S isotopic data of Baoshan Cu–Pb–Zn deposit

Sample	Mineral	$\delta^{34}\text{S}/\text{‰}$	Type	Sample	Mineral	$\delta^{34}\text{S}/\text{‰}$	Type
BS451-3-1	Pyrite	3.76	Py I	BS724-6-6	Pyrite	3.92	W_Py
BS451-3-2	Pyrite	3.83	Py I	BS729-2-1	Pyrite	5.33	N_Py
BS451-3-3	Pyrite	3.98	Py I	BS729-2-2	Pyrite	4.93	N_Py
BS451-3-4	Pyrite	3.93	Py I	BS729-2-3	Pyrite	5.86	N_Py
BS451-3-5	Pyrite	3.92	Py I	BS729-2-4	Pyrite	5.8	N_Py
BS451-1-1	Pyrite	4.29	Py II	BS729-2-5	Pyrite	5.37	N_Py
BS451-1-2	Pyrite	4.43	Py II	BS472-1	Sphalerite	7.53	SK_Sp
BS451-1-3	Pyrite	4.53	Py II	BS472-2	Sphalerite	7.12	SK_Sp
BS451-1-4	Pyrite	4.07	Py II	BS472-3	Sphalerite	6.77	SK_Sp
BS451-1-5	Pyrite	4.59	Py II	BS472-4	Sphalerite	6.07	SK_Sp
BS451-1-6	Pyrite	3.85	Py II	BS472-5	Sphalerite	6.11	SK_Sp
BS451-1-7	Pyrite	4.03	Py III	BS801-10-6	Sphalerite	4.6	C_Sp
BS451-1-8	Pyrite	4.52	Py III	BS801-10-7	Sphalerite	4.33	C_Sp
BS451-1-9	Pyrite	4.44	Py III	BS801-10-8	Sphalerite	3.64	C_Sp
BS451-1-10	Pyrite	4.04	Py III	BS801-10-9	Sphalerite	4.44	C_Sp
BS451-3-11	Pyrite	4.62	Py III	BS801-10-10	Sphalerite	3.41	C_Sp
BS801-10-1	Pyrite	4.7	C_Py	BS724-6-7	Sphalerite	4.79	W_Sp
BS801-10-2	Pyrite	4.25	C_Py	BS724-6-8	Sphalerite	5	W_Sp
BS801-10-3	Pyrite	4.28	C_Py	BS724-6-9	Sphalerite	4.99	W_Sp
BS801-10-4	Pyrite	4.13	C_Py	BS724-6-10	Sphalerite	5.21	W_Sp
BS801-10-5	Pyrite	4.42	C_Py	BS724-6-11	Sphalerite	5	W_Sp
BS724-6-1	Pyrite	5.02	W_Py	BS729-2-6	Sphalerite	4.97	N_Sp
BS724-6-2	Pyrite	5.74	W_Py	BS729-2-7	Sphalerite	4.87	N_Sp
BS724-6-3	Pyrite	5.2	W_Py	BS729-2-8	Sphalerite	4.87	N_Sp
BS724-6-4	Pyrite	1.85	W_Py	BS729-2-9	Sphalerite	5.23	N_Sp
BS724-6-5	Pyrite	2.87	W_Py	BS729-2-10	Sphalerite	4.78	N_Sp

negative signs. The angles of the arrows highlight the four elements clusters (Fig. 9(a)), which provide a reference for revealing the correlations among the elements. The adjacent points indicate similarities in the trace element compositions.

In addition, the disseminated pyrite with a euhedral texture can be considered to be formed primarily from magmatic materials [39]. Therefore, this type of pyrite from the granodiorite porphyry without sulfide veinlets was plotted on the PC2 vs PC1 plane for comparison. The evolution trends of the pyrite based on the element compositions and generations of pyrite are shown in Fig. 9.

5 Discussion

5.1 Trace element compositions of pyrite

The time-resolved depth profiles (Fig. 10) and

element clusters from the PCA (Fig. 9(a)) indicate that Co, Ni, As, and Se may occur as solid solutions, whereas Mn, Zn, Mo, Ag, Sb, Te, Au, Tl, Pb, and Bi occur as mineral inclusions and/or solid solutions. The strong correlation between Mn and Mo, especially the highest values in the colloform pyrite (Py II), implies the occurrence of Mn hydroxides, which were absorbed by pyrite (Fig. 10) [40,41]. The Cd and minor Cu are primarily related to the sphalerite inclusions [42]. The wide variation in the Pb concentrations and synchronous correlation with Ag and Sb indicate the occurrence of andorite and/or boulangerite inclusions (Fig. 10) [43,44].

The Co/Ni ratio is considered an important index for identifying the origin of pyrite [45,46]. The Co/Ni ratios of the Py I are 0.85–9.61 (average 2.78), indicating that the Py I is related to hydrothermal fluids [47]. However, the contents of

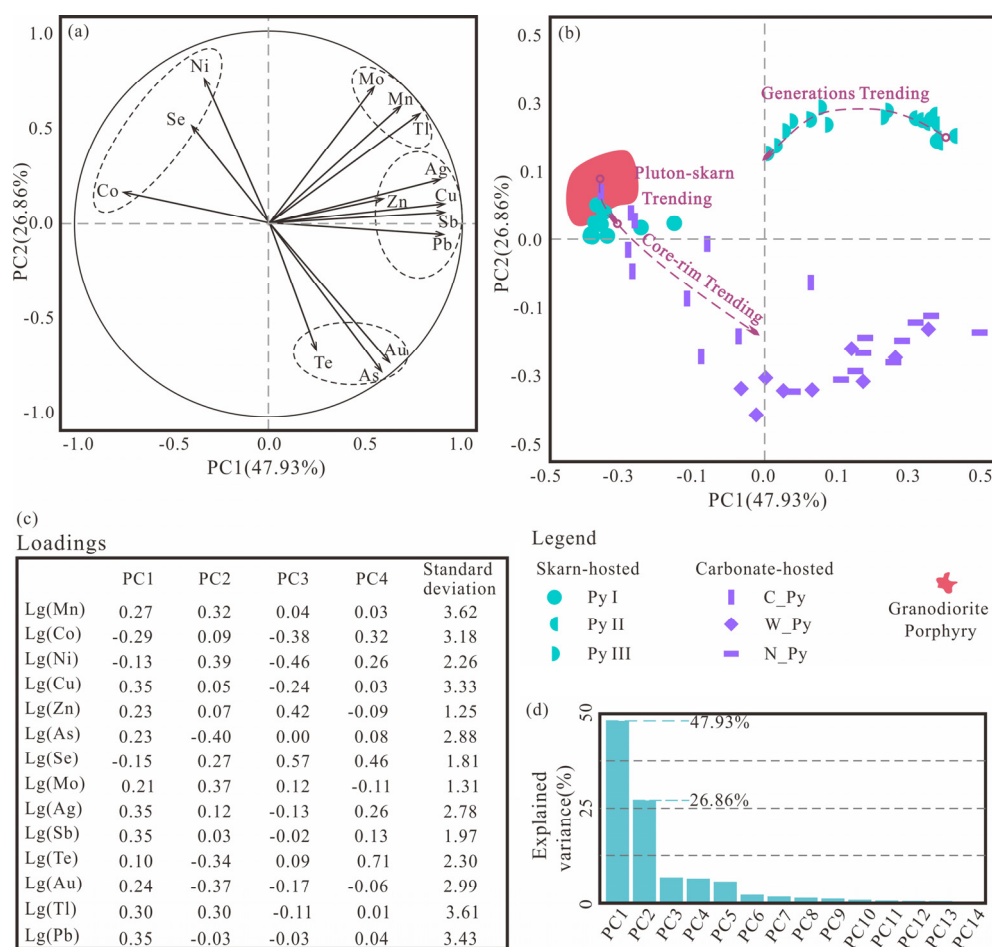


Fig. 9 Principal component analysis (PCA) of In-transformed LA-ICP-MS trace element compositions of pyrite from Baoshan deposit: (a) Loading plot of PCA showing elements and highlighted groups of elements with similar behaviors; (b) Score plot of all of points in PC1 and PC2 for trace element compositions of six pyrite species; (c) Loadings of principal components (PC1–PC4, explaining 87.39% of total variance); (d) Scree plot of eigenvalues of correlation matrix explaining variance

either Co or Ni are below the detection limit for the other types of pyrite, which is an obstacle to determining their origins (Fig. 7 and Table 2). HANLEY et al [48] suggested that Co can precipitate with Cu due to decreasing temperature, and it is only enriched in the pyrite that forms earlier than chalcopyrite. In the Baoshan deposit, the sphalerite intergrown with the chalcopyrite has high Co contents (up to 0.26 wt.%), which may have depleted the Co in the hydrothermal system [21].

As a characteristic element of colloform pyrite (Py II), the Py III was also found to have high Mn contents, suggesting that the texture of the pyrite is not the dominant factor for the concentration of Mn. Mn has been reported to precipitate at low temperatures, and fluid mixing can be another factor determining its precipitation [49]. Moreover,

the As concentration is a function of temperature and is enriched in pyrite at low temperatures [50]. The coupling of Mn and As in the skarn-hosted pyrite (Py I, Py II, and Py III) indicates a decreasing temperature trend, which may have been triggered by the fluid mixing process (Figs. 7 and 9(b)).

However, the decoupling of Mn and As in the carbonate-hosted pyrite (C_Py, W_Py, and N_Py) indicates that the temperature was no longer the dominant factor, suggesting a transformation of the physicochemical conditions (Figs. 7 and 9(b)). The Se contents may have recorded this transformation, and they should have the opposite trend due to their different temperature responses [40]. The wide range of As and Se contents and the oscillatory zoning of the C_Py indicate a relatively slow crystallization process during temperature and $f(\text{O}_2)$ fluctuations due to the intermittent pulses of the

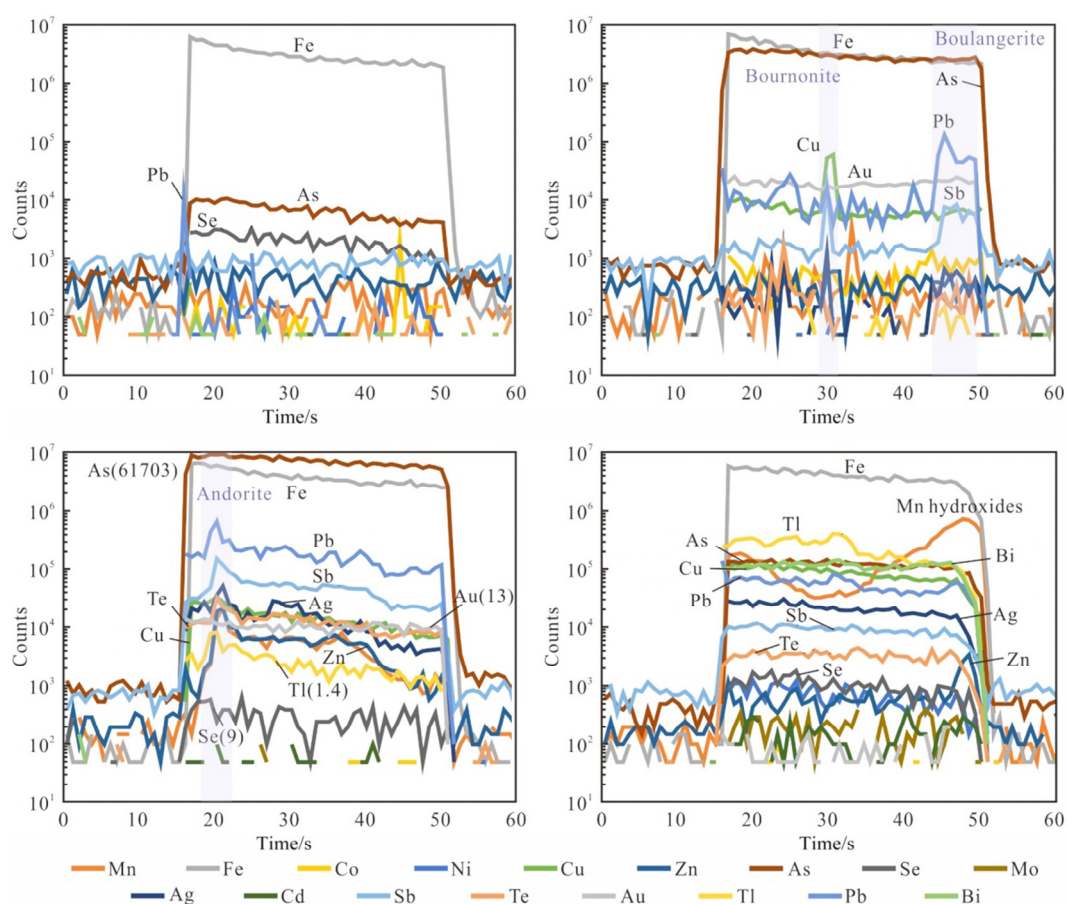


Fig. 10 Representative time-resolved depth profiles for selected elements in pyrite

ore-forming fluids related to the magmatism (Figs. 6(g) and 7) [46]. The W_{Py} and N_{Py} have the highest As and the lowest Se contents, suggesting that they were formed under the lowest temperature conditions. However, the sphalerite geothermometers indicate that these vein-type ores had similar ore-forming temperatures [21,35]. Thus, it can be inferred that compared to the changes in temperature, the $f(O_2)$ decreased more significantly, which implies more extensive water–rock interactions [49].

The average Bi content of the strata of the Nanling region is approximately 1.9–2.9 times higher than that of continental crust [51]. The concentration of Bi (>1 ppm) in the pyrite reflects a sedimentary contribution to the hydrothermal system [41,52]. In the Baoshan deposit, the average of Bi content is 0.54 ppm, indicating that the sedimentary strata contributed little to the mineralization. In addition, the abundance of Te in the pyrite suggests that the ore-forming fluid was associated with the magmatic system. The Te/Au

ratios of all of the types of pyrite in the Baoshan deposit (0.02–646) are similar to those of pyrite precipitated from magmatic hydrothermal systems ($Te/Au > 1$) [53–55], also demonstrating their magmatic hydrothermal affinity.

5.2 Colloform pyrite and fluid mixing

Colloform pyrite, which can occur during synsedimentary processes or can precipitate in hydrothermal systems, contains a great deal of information and can record the physicochemical conditions and fluid evolution processes. Its disequilibrium texture is considered to be formed by rapid nucleation and crystallization, implying abrupt changes in physicochemical conditions due to supercooled or supersaturated processes [41,56]. In addition, microbial activity may be another factor that can result in the formation of colloform pyrite [57].

In the Baoshan deposit, the median Co/Ni (<0.01), Cu/Ni (>90), As/Ni (>70), and Ag/Au (>410) ratios of the Py II (colloform pyrite; Table 2

and Fig. 7) are outside of the ranges defined for diagenetic pyrite [58]. Furthermore, its $\delta^{34}\text{S}$ values ((3.85–4.59)‰) also indicate a hydrothermal origin related to magmatism without microbial activity. As mentioned previously, there are significant differences in most of the trace element concentrations of the Py I and Py II, which cannot be explained by temperature fluctuations or the evolution of a single fluid. Significantly, the concentrations of the temperature sensitive elements (e.g., As, Se, and Tl) in the Py II, which are distinctly different from those in the Py I but vary over a narrow range (Fig. 7), indicate a sharp decrease in the temperature of the hydrothermal system. In addition, Tl has a strong affinity for magmatic vapors due to its volatile nature [42,49], and it is considered to escape from the hydrothermal fluid when boiling. Fluid boiling will significantly affect the stability of the Au-bisulfide complex and result in its precipitation [59]. However, the extremely high Tl (up to 112 ppm) and low Au (<0.132 ppm) concentrations of the Py II indicate that significant fluid boiling may not have occurred during its crystallization. Therefore, it can be concluded that the Py II was rapidly precipitated due to a sudden drop in temperature caused by the fluid mixing [41]. Moreover, the decrease in temperature and dilution of the Cl^- concentration were favorable for Zn and Pb, which migrated in the solution as chlorine complexes precipitated, and were incorporated into Py II [60]. The PCA results also indicate the occurrence of this fluid mixing process (Fig. 9(b)). There are two evolutionary paths for the trace elements in the types of pyrite in the Baoshan deposit, i.e., (1) from granodiorite porphyry to Py I to C_Py, and (2) from Py II to Py III (to Py I). This suggests that the precipitation conditions of the Py III were between those of the Py I and Py II, which is the same as a neutralization process of two endmember conditions during fluid mixing.

5.3 Source of sulfur

Sulfur isotope compositions have been widely used to constrain the genesis of deposits and can be used to efficiently distinguish different sources of sulfur (e.g., mantle sulfur, marine sulfate, and biogenic sulfur) [61–66]. In this study, in-situ sulfur isotope analysis was utilized to identify the sulfur

source of different types of pyrite in the Baoshan deposit (Fig. 8 and Table 3). The absence of sulfate minerals indicates that the $\delta^{34}\text{S}$ of the sulfides approximately represents the total S isotope composition of the hydrothermal system in the Baoshan deposit [67,68]. S isotope fractionation did not strictly obey the thermodynamic equilibrium fractionation processes: $\delta^{34}\text{S}_{\text{molybdenite}} > \delta^{34}\text{S}_{\text{pyrite}} > \delta^{34}\text{S}_{\text{sphalerite}} > \delta^{34}\text{S}_{\text{galena}}$ [6]. Even for the $\delta^{34}\text{S}_{\text{pyrite}} > \delta^{34}\text{S}_{\text{sphalerite}}$ in the carbonate-hosted ores, the temperature calculated using the pyrite-sphalerite sulfur isotopic geothermometer is higher than the reasonable formation temperature of sulfides, indicating the occurrence of kinetic fractionation between the sulfides and the ore-forming fluids [67,69].

As mentioned previously, there was a fluid mixing process between the Py I and Py II (Figs. 7 and 9), which was also recorded by the sulfur isotope data, i.e., the apparent differences in their $\delta^{34}\text{S}$ values (Table 3 and Fig. 8). The $\delta^{34}\text{S}$ values of the sphalerite in the skarn-hosted ore (SK_Sp), which is intergrown with the chalcopyrite (later than the Py I but earlier than the Py II), are higher than those of any of the types of pyrite, implying that the mixed fluid may have had higher $\delta^{34}\text{S}$ values. The $\delta^{34}\text{S}$ values of the Py I are within the narrow range of (3.76–3.98)‰ and are close to those of granodiorite porphyry ((1.5–3.5)‰) [16]. However, the $\delta^{34}\text{S}$ values ((3.85–4.62)‰) of the Py II and Py III have a relatively wide range and are slightly higher than those of the disseminated pyrite within the granodiorite porphyry but are still within the range of the S isotope composition of the magma [70]. The $\delta^{34}\text{S}$ values of the C_Py ((3.4–4.7)‰) are similar to those of the Py II and Py III, indicating that they had the same sulfur sources. However, the higher $\delta^{34}\text{S}$ values of the W_Py and N_Py (>5‰) may result from the involvement of heavier isotopes [71] or lower $f(\text{O}_2)$ conditions due to mineralization of Fe-oxides [56] or extensive water–rock reactions with the carbonate host rocks [49]. The $\delta^{13}\text{C}_{\text{V-PDB}}$ and $\delta^{18}\text{O}_{\text{V-SMOW}}$ values of the calcite samples have demonstrated that this interaction occurred [18] and the ore-hosting strata (Zimenqiao Formation) of the W_Py and N_Py may have the potential to provide evaporite sulfur with very high $\delta^{34}\text{S}$ values [6,16].

5.4 Implication for mineralization of Baoshan deposit

The δD (from -64% to -86%) and $\delta^{18}O$ (from 7.47% to 0.33%) values of the ore-forming fluids in the Baoshan deposit indicate mixing of magmatic water with meteoric water, especially for the vein-type ores [72]. SHU et al [60] demonstrated that fluid mixing is a significant precipitation mechanism in Pb–Zn mineralization. Based on the above discussion, fluid mixing, which is demonstrated by the trace element compositions and sulfur isotopes of the pyrite, played an essential role in the mineralization in the Baoshan deposit.

During 170–160 Ma, lithospheric extension and crustal thinning resulting from the mantle–crust interactions caused by the subduction of the Paleo-Pacific Plate extended inland into the South China Block [12,26]. Under this tectonic regime, the granodiorite porphyry magma, which has a high-K calc-alkaline signature with mafic magmatic enclaves, was derived from the anatexis of Paleoproterozoic crustal material induced by injection or underplating of mantle-derived magmas [34,73]. The Cu was predominantly derived from the modified mantle and re-melting of the Neoproterozoic relict island arc [34]. During the assimilation process, the magmas absorbed Pb and Zn from the metamorphosed basement [6,11,15], which was also recorded by the trace element compositions of the sphalerite [21].

Thus, Cu-, Pb-, Zn-rich magmas may have intruded into the Carboniferous Shidengzi Formation limestone and the Zimenqiao Formation dolomite, which were controlled by the Baoling inversion anticline and faults (e.g., F₂₁, F₂₅), respectively (Fig. 11(a)). Subsequently, the magmatic-hydrothermal fluids ascended along the faults and interlayer slip surface in the Middle-Late Jurassic (Fig. 11(b)) ((162.6±2.9) Ma, U-Pb age for the garnet) [31], which led to skarn alteration and precipitation of the Py I (Fig. 11(c)). The accumulation in pressure resulted in hydraulic fracturing accompanied by a transition from lithostatic pressure to hydrostatic pressure [72,74] and the formation of breccia (Fig. 5(a)), which provided beneficial pathways for meteoric water (Figs. 5(a) and 11(d)). In this case, the sudden release of the pressure and the sharp decrease in the temperature triggered by the hydraulic fracturing and mixing of meteoric water led to the rapid

crystallization of the Py II with a colloform texture [75]. In addition, Cu prefers to be transported as chloride complexes, and near-neutral pH and oxidizing conditions can increase its solubility [76–78]. The changes in the $f(O_2)$ and pH conditions caused by the local boiling, water–rock interactions, and mineralization of Fe-oxides (magnetite) resulted in Cu supersaturation and precipitation from the hydrothermal system (Fig. 11(e)) [59,70,79]. With further mixing of the ore-forming fluids and meteoric water, the composition of the Py III gradually approached that of the Py I (Fig. 9(b)) and generated Pb–Zn ore-bodies locally (Fig. 11(e)). The fluctuations in the temperature and $f(O_2)$ conditions may have been triggered by intermittent pulses of ore-forming fluids, which formed the C_Py with growth bands [46]. Thus, the elements (e.g., As and Se) precipitated intermittently with the hydrothermal pulses and formed enriched or depleted bands in the C_Py.

Coevally, when this ore-forming fluid was blocked by the sandstone of the Ceshui Formation and flowed into F₂₁ through the fluid escape structures (Figs. 5(b, c) and 11(e)), extensive boiling occurred due to the fluid mixing with a larger amount of meteoric water and the pressure release as it entered the fault, which is supported by the fluid inclusion data [72]. A previous study suggested that the Baoshan vein-type Pb–Zn mineralization was formed under relatively high pH conditions [21], in which the Au predominantly migrated as $Au(HS)_2^-$ [80,81]. Thus, the fluid boiling was favorable for the precipitation of Au and As due to the volatilization of O₂, H₂ and H₂S [59,82]. Moreover, the extensive water–rock reactions resulted in a decrease in the $f(O_2)$ of the ore-forming fluid due to the oxidation of Fe²⁺, which was conducive to the precipitation of Te [18,83,84]. During these processes, As, Au and Te precipitated from the hydrothermal fluids and were incorporated into the pyrite (W_Py and N_Py). The decrease in the Cl⁻ concentration triggered by the fluid mixing resulted in the precipitation of Pb and Zn from the ore-forming fluid [60] and the hydrothermal vein-type Pb–Zn mineralization was formed along the faults. Finally, the ore-forming fluid reached the surface and generated the Fe–Mn oxides (Fig. 11(e)).

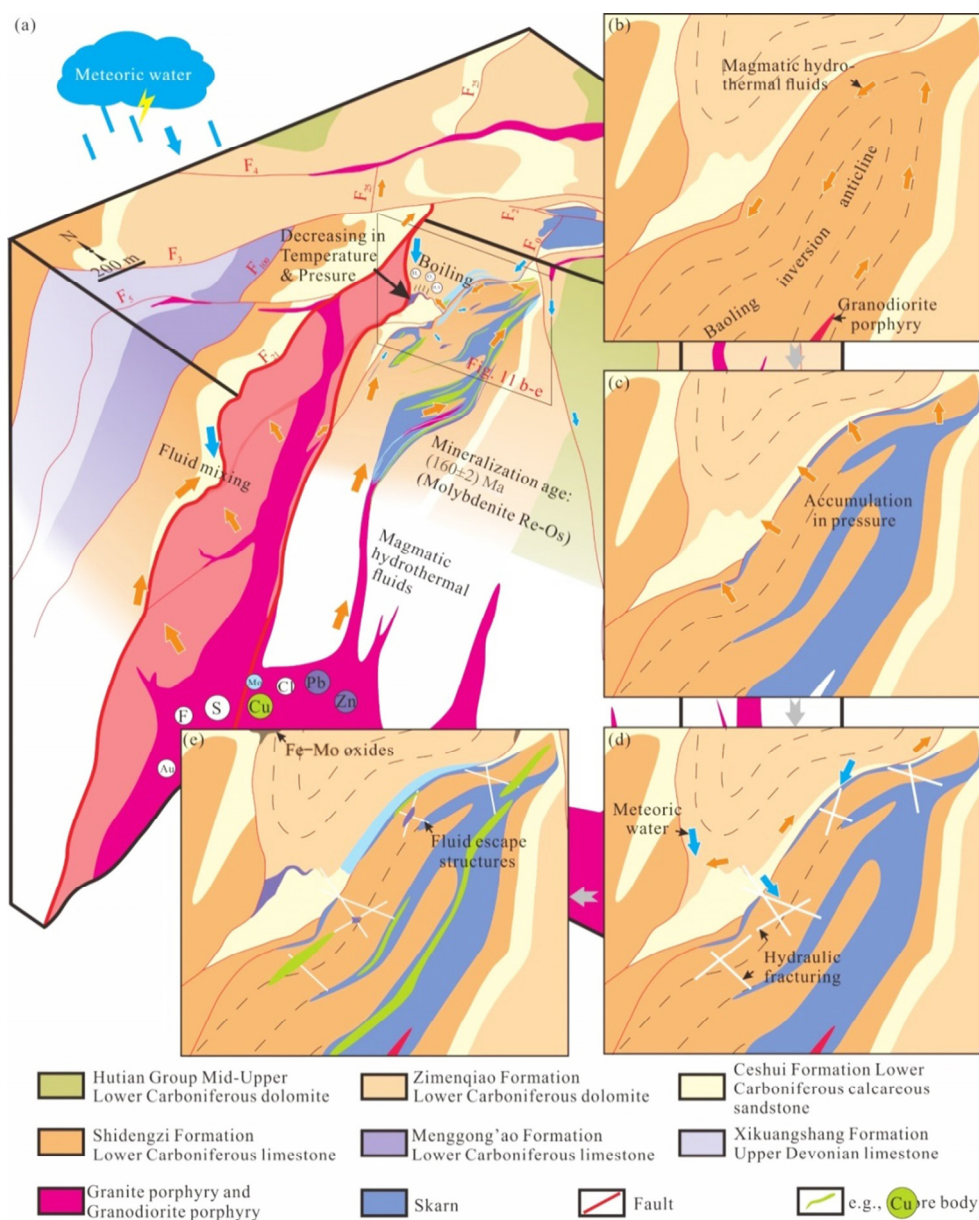


Fig. 11 Schematic diagram of mineralization model of Baoshan deposit

6 Conclusions

(1) Based on the generation relationship and trace element compositions, the PCA revealed the characteristics of the trace element compositions, highlighted the correlations among the elements, and revealed the evolution processes of the trace element composition of the minerals, which provide new insights into the application of PCA to the trace element geochemistry of minerals.

(2) Two evolution trends for the trace element compositions of the pyrite in the Baoshan deposit were identified by PCA. Their intersection provides

trace element geochemical based information about the fluid mixing process.

(3) The sulfur of Cu mineralization system is predominantly derived from the magma, whereas that of Pb–Zn mineralization is derived from magma and host rocks.

(4) Fluid mixing, boiling, and water–rock interactions played important role in the mineralization at the Baoshan deposit. The occurrence of Fe–Mo oxides on the surface can serve as an indicator of deep mineralization.

Acknowledgments

We thank Ms. Xiu WEN and Mr. Yang XIAO

(Guangzhou Tuoyan Testing Technology Co., Ltd., China) for their assistance and guidance during the LA-ICP-MS analyses. We thank Ms. Jian-mei TANG (Beijing Createch Testing Technology Co., Ltd. China) for the sulfur isotope analyses. We would like to thank Prof. Yu ZHANG (Central South University, Changsha, China) for his valuable suggestions for improving this contribution. This research was funded by the National Key Research and Development Program of China (Nos. 2018YFC0603904, 2018YFC0603901).

Supplementary data

The complete LA-ICP-MS data of pyrite from the Baoshan deposit described in this work can be found at: <http://www.ysxbcn.com/download/TNMSC-2021-1217.pdf>

References

- [1] ZHAO L J, ZHANG Y, SHAO Y J, LI H B, AHMAD SHAH S, ZHOU W J. Using garnet geochemistry discriminating different skarn mineralization systems: Perspective from Huangshaping W–Mo–Sn–Cu polymetallic deposit, South China [J]. *Ore Geology Reviews*, 2021, 138: 104412.
- [2] ZHAO Z, FU T Y, GAN J W, LIU C, WANG D H, SHENG J F, LI W B, WANG P G, YU Z F, CHEN Y C. A synthesis of mineralization style and regional distribution and a proposed new metallogenic model of Mesozoic W-dominated polymetallic deposits in South China [J]. *Ore Geology Reviews*, 2021, 133: 104008.
- [3] XU J W, LAI J Q, LI B, LU A H, ROCHOLL A, DICK J M, PENG J T, WANG K L. Tungsten mineralization during slab subduction: A case study from the Huxingshan deposit in northeastern Hunan Province, South China [J]. *Ore Geology Reviews*, 2020, 124: 103657.
- [4] ZHANG Y, SHAO Y J, LIU Q Q, CHEN H Y, QUAN W, SUN A X. Jurassic magmatism and metallogeny in the eastern Qin-Hang Metallogenic Belt, SE China: An example from the Yongping Cu deposit [J]. *Journal of Geochemical Exploration*, 2018, 186: 281–297.
- [5] CAO J Y, WU Q H, YANG X Y, DENG X T, LI H, KONG H, XI X S. Geochemical factors revealing the differences between the Xitian and Dengfuxian composite plutons, middle Qin-Hang Belt: Implications to the W–Sn mineralization [J]. *Ore Geology Reviews*, 2020, 118: 103353.
- [6] LI H, KONG H, ZHOU Z K, WU Q H, XI X S, GABORATIO J A S. Ore-forming material sources of the Jurassic Cu–Pb–Zn mineralization in the Qin–Hang ore belt, South China: Constraints from S–Pb isotopes [J]. *Geochemistry*, 2019, 79: 280–306.
- [7] WANG D H, HUANG F, WANG Y, HE H H, LI X M, LIU X X, SHENG J F, LIANG T. Regional metallogeny of Tungsten-tin-polymetallic deposits in Nanling region, South China [J]. *Ore Geology Reviews*, 2020, 120: 103305.
- [8] LEGROS H, HARLAUX M, MERCADIER J, ROMER R L, POUJOL M, CAMACHO A, MARIGNAC C, CUNEY M, WANG R C, CHARLES N, LESPINASSE M Y. The world-class Nanling metallogenic belt (Jiangxi, China): W and Sn deposition at 160 Ma followed by 30 m.y. of hydrothermal metal redistribution [J]. *Ore Geology Reviews*, 2020, 117: 103302.
- [9] QU H Y, MAO J W, ZHOU S M. Metallogenesis of stratiform Cu mineralization in the Dabaoshan polymetallic deposit, Northern Guangdong Province, South China [J]. *Journal of Geochemical Exploration*, 2020, 210: 106448.
- [10] LIU X, WANG Q, MA L, WYMAN D A, ZHAO Z H, YANG J H, ZI F, TANG G J, DAN W, ZHOU J S. Petrogenesis of Late Jurassic Pb–Zn mineralized high $\delta^{18}\text{O}$ granodiorites in the western Nanling Range, South China [J]. *Journal of Asian Earth Sciences*, 2020, 192: 104236.
- [11] ZHAO P L, YUAN S D, MAO J W, SANTOSH M, ZHANG D L. Zircon U–Pb and Hf–O isotopes trace the architecture of polymetallic deposits: A case study of the Jurassic ore-forming porphyries in the Qin-Hang metallogenic belt, China [J]. *Lithos*, 2017, 292/293: 132–145.
- [12] LI S Z, SUO Y H, LI X Y, ZHOU J, SANTOSH M, WANG P C, WANG G Z, GUO L L, YU S Y, LAN H Y, DAI L M, ZHOU Z Z, CAO X Z, ZHU J J, LIU B, JIANG S H, WANG G, ZHANG G W. Mesozoic tectono-magmatic response in the East Asian ocean-continent connection zone to subduction of the Paleo-Pacific Plate [J]. *Earth-Science Reviews*, 2019, 192: 91–137.
- [13] REN L, BAO Z W, HUANG W T, LIN S P, XIE S X, LIAO J, LI J, LIANG H Y. Flat-slab subduction and formation of “intraplate” porphyry deposits: Insights from the Jurassic high and low La/Yb ore-forming porphyries along the Qin-Hang belt, South China [J]. *Ore Geology Reviews*, 2020, 123: 103574.
- [14] MI J R, YUAN S D, YUAN Y B, XUAN Y S. Mineralogical characteristics and indicative significance of biotite in granodiorite porphyry of Baoshan deposit in Southern Hunan province [J]. *Mineral Deposits*, 2014, 33: 1357–1365. (in Chinese)
- [15] LU Y F, MA L Y, QU W J, MEI Y P, CHEN X Q. U–Pb and Re–Os isotope geochronology of Baoshan Cu–Mo polymetallic ore deposit in Hunan province [J]. *Acta Petrologica Sinica*, 2006, 22: 2483–2492. (in Chinese)
- [16] DING T, MA D S, LU J J, ZHANG R Q, XIE Y C. Sulfur and lead isotopic compositions of granitoids and fluid inclusions in Baoshan deposit, Hunan Province [J]. *Mineral Deposits*, 2016, 35: 663–676. (in Chinese)
- [17] MI J R, YUAN S D, XUAN Y S, ZHANG D L. Zircon U–Pb ages, Hf isotope and trace element characteristics of the granodiorite porphyry from the Baoshan–Dafang ore district, Hunan: Implications for regional metallogeny [J]. *Acta Petrologica Sinica*, 2018, 34: 2548–2564. (in Chinese)
- [18] XIE Y C, LU J J, YANG P, MA D S, YAO Z W, ZHANG R Q, CAI Y, DING T. S, Pb, C and O isotopic characteristics and sources of metallogenic materials of Baoshan Pb–Zn deposit, southern Hunan Province [J]. *Mineral Deposits*, 2015, 34: 333–351. (in Chinese)
- [19] BAO T, TE L, YANG Y L, LI Z L. Characteristics of sulfur isotope geochemistry of Baoshan Cu–Mo–Pb–Zn–Ag polymetallic deposit, Hunan Province and its geological

- significance [J]. *Acta Mineralogica Sinica*, 2014, 34: 261–266. (in Chinese)
- [20] YAO J M, HUA R M, LIN J F. REE, Pb-S isotope geochemistry and Rb–Sr isochron age of pyrites in the Baoshan deposit, south Hunan Province, China [J]. *Acta Petrologica Sinica*, 2006, 80: 1045–1054. (in Chinese)
- [21] ZHANG J K, SHAO Y J, LIU Z F, CHEN K. Sphalerite as a record of metallogenic information using multivariate statistical analysis: Constraints from trace element geochemistry [J]. *Journal of Geochemical Exploration*, 2022, 232: 106883.
- [22] ZHOU Y Z, ZHENG Y, LIN Z W, ZENG C Y, LI X Y, LIU J, YU P P, CHEN S. Evolution and mineralization of the Qin-Hang Belt [J]. *Ore Deposit Geology*, 2014, 33: 995–996.
- [23] ZHOU Y Z, LI X Y, ZHENG Y, SHEN W J, HE J G, YU P P, NIU J, ZENG C Y. Metallogenic geological background and metallogenic regularities of the Qinghang joint belt [J]. *Acta Petrologica Sinica*, 2017, 33: 667–681. (in Chinese)
- [24] LI X H, LI W X, LI Z X, LO C H, WANG J, YE M F, YANG Y H. Amalgamation between the Yangtze and Cathaysia Blocks in South China: Constraints from SHRIMP U-Pb zircon ages, geochemistry and Nd–Hf isotopes of the Shuangxiwu volcanic rocks [J]. *Precambrian Research*, 2009, 174: 117–128.
- [25] SHU L S, YAO J L, WANG B, FAURE M, CHARVET J, CHEN Y. Neoproterozoic plate tectonic process and Phanerozoic geodynamic evolution of the South China Block [J]. *Earth-Science Reviews*, 2021, 216: 103596.
- [26] MAO J W, CHENG Y B, CHEN M H, PIRAJNO F. Major types and time–space distribution of Mesozoic ore deposits in South China and their geodynamic settings [J]. *Mineralium Deposita*, 2013, 48: 267–294.
- [27] MAO J W, PIRAJNO F, COOK N. Mesozoic metallogeny in East China and corresponding geodynamic settings—An introduction to the special issue [J]. *Ore Geology Reviews*, 2011, 43: 1–7.
- [28] ZHAO X, LI N B, HUIZENGA J M, YAN S, YANG Y Y, NIU H C. Rare earth element enrichment in the ion-adsorption deposits associated granites at Mesozoic extensional tectonic setting in South China [J]. *Ore Geology Reviews*, 2021, 137: 104317.
- [29] ZHANG X, NI P, WANG G G, JIANG Y H, JIANG D S, LI S N, FAN M S. Petrogenesis and oxidation state of granodiorite porphyry in the Jurassic Chuankeng skarn Cu deposit, South China: Implications for the Cu fertility and mineralization potential [J]. *Journal of Asian Earth Sciences*, 2020, 191: 104184.
- [30] ZHOU X M, SUN T, SHEN W Z, SHU L S, NIU Y L. Petrogenesis of Mesozoic granitoids and volcanic rocks in South China: A response to tectonic evolution [J]. *Episodes*, 2006, 29: 26–33.
- [31] LI D F, TAN C Y, MIAO F Y, LIU Q F, ZHANG Y, SUN X M. Initiation of Zn–Pb mineralization in the Pingbao Pb–Zn skarn district, South China: Constraints from U-Pb dating of grossular-rich garnet [J]. *Ore Geology Reviews*, 2019, 107: 587–599.
- [32] MEINERT L D, DIPPLE G M, NICOLESCU S. World skarn deposits [M]//*Economic Geology*. Economic Geology 100th Anniversary Volume. 2005: 299–336.
- [33] KONG H, LI H, WU Q H, XI X S, DICK J M, GABO-RATIO J A S. Co-development of Jurassic I-type and A-type granites in southern Hunan, South China: Dual control by plate subduction and intraplate mantle upwelling [J]. *Geochemistry*, 2018, 78: 500–520.
- [34] XIE Y C, LU J J, MA D S, ZHANG R Q, GAO J F, YAO Y. Origin of granodiorite porphyry and mafic microgranular enclave in the Baoshan Pb–Zn polymetallic deposit, southern Hunan Province: Zircon U–Pb chronological, geochemical and Sr–Nd–Hf isotopic constraints [J]. *Acta Petrologica Sinica*, 2013, 29: 4186–4214. (in Chinese)
- [35] FRENZEL M, HIRSCH T, GUTZMER J. Gallium, germanium, indium, and other trace and minor elements in sphalerite as a function of deposit type — A meta-analysis [J]. *Ore Geology Reviews*, 2016, 76: 52–78.
- [36] PEDREGOSA F, VAROQUAUX G, GRAMFORT A, MICHEL V, THIRION B, GRISEL O, BLONDEL M, MÜLLER A, NOTHMAN J, LOUPPE G. Scikit-learn: Machine learning in python [J]. *Journal of Machine Learning Research*, 2012, 12: 2825–2830.
- [37] QI F Y. Magmatic-fluvial metallogenesis and its evolution in Baoshan Cu–Pb–Zn polymetallic deposit, Hunan Province [D]. China University of Geosciences, 2012: 1–100. (in Chinese)
- [38] DING T, MA D S, LU J J, ZHANG R Q, ZHANG S T. S, Pb, and Sr isotope geochemistry and genesis of Pb–Zn mineralization in the Huangshaping polymetallic ore deposit of southern Hunan Province, China [J]. *Ore Geology Reviews*, 2016, 77: 117–132.
- [39] ISHIHARA S, WANG P G, KAJIWARA Y, WATANABE Y. Origin of sulfur in some magmatic-hydrothermal ore deposits of South China [J]. *Bulletin of the Geological Survey of Japan*, 2003, 54: 161–169.
- [40] MASLENNIKOV V V, MASLENNIKOVA S P, LARGE R R, DANYUSHEVSKY L V. Study of trace element zonation in vent chimneys from the silurian Yaman-Kasy volcanic-hosted massive sulfide deposit (Southern Urals, Russia) using laser ablation-inductively coupled plasma mass spectrometry (LA-ICPMS) [J]. *Economic Geology*, 2009, 104: 1111–1141.
- [41] KEITH M, HÄCKEL F, HAASE K M, SCHWARZ-SCHAMPERA U, KLEMD R. Trace element systematics of pyrite from submarine hydrothermal vents [J]. *Ore Geology Reviews*, 2016, 72: 728–745.
- [42] DEDITIUS A P, REICH M. Constraints on the solid solubility of Hg, Tl, and Cd in arsenian pyrite [J]. *American mineralogist*, 2016, 101: 1451–1459.
- [43] CHEN F C, DENG J, WANG Q F, HUIZENGA J M, LI G J, GU Y W. LA-ICP-MS trace element analysis of magnetite and pyrite from the Hetaoping Fe–Zn–Pb skarn deposit in Baoshan block, SW China: Implications for ore-forming processes [J]. *Ore Geology Reviews*, 2020, 117: 103309.
- [44] COOK N J, CIOBANU C L, PRING A, SKINNER W, SHIMIZU M, DANYUSHEVSKY L, SAINI-EIDUKAT B, MELCHER F. Trace and minor elements in sphalerite: A LA-ICPMS study [J]. *Geochimica et Cosmochimica Acta*, 2009, 73: 4761–4791.
- [45] GREGORY D D, LARGE R R, BATH A B, STEADMAN J A, WU S, DANYUSHEVSKY L, BULL S W, HOLDEN P, IRELAND T R. Trace element content of pyrite from the Kapai Slate, St. Ives Gold District, Western Australia [J].

Economic Geology, 2016, 111: 1297–1320.

- [46] LARGE R R, HALPIN J A, DANYUSHEVSKY L V, MASLENNIKOV V V, BULL S W, LONG J A, GREGORY D D, LOUNEJEVA E, LYONS T W, SACK P J, MCGOLDRICK P J, CALVER C R. Trace element content of sedimentary pyrite as a new proxy for deep-time ocean–atmosphere evolution [J]. *Earth and Planetary Science Letters*, 2014, 389: 209–220.
- [47] REICH M, SIMON A C, DEDITIUS A, BARRA F, CHRYSSOULIS S, LAGAS G, TARDANI D, KNIPPING J, BILENKER L, SÁNCHEZ-ALFARO P, ROBERTS M P, MUNIZAGA R. Trace element signature of pyrite from the Los Colorados iron oxide-apatite (IoA) deposit, Chile: A missing link between andean ioa and iron oxide copper-gold systems? [J]. *Economic Geology*, 2016, 111: 743–761.
- [48] HANLEY J, MACKENZIE M, WARREN M, GUILLONG M. Distribution and origin of platinum-group elements in alkalic porphyry Cu–Au and low sulfidation epithermal Au deposits in the Canadian Cordillera [C]//11th International Platinum Symposium. Sudbury: Ontario Geological Survey, 2010: 21–24.
- [49] KEITH M, SMITH D J, JENKIN G R T, HOLWELL D A, DYE M D. A review of Te and Se systematics in hydrothermal pyrite from precious metal deposits: Insights into ore-forming processes [J]. *Ore Geology Reviews*, 2018, 96: 269–282.
- [50] XING Y L, BRUGGER J, TOMKINS A, SHVAROV Y. Arsenic evolution as a tool for understanding formation of pyritic gold ores [J]. *Geology*, 2019, 47: 335–338.
- [51] GU L X, ZAW K, HU W X, ZHANG K J, NI P, HE J X, XU Y T, LU J J, LIN C M. Distinctive features of Late Palaeozoic massive sulphide deposits in South China [J]. *Ore Geology Reviews*, 2007, 31: 107–138.
- [52] XIE J C, GE L K, FANG D, LI Q Z, QIAN L, LI Z S, YAN J, SUN W D. Geochemistry of pyrite from stratabound massive sulfide deposits, Tongling region, China: Implication for their genesis [J]. *Ore Geology Reviews*, 2020, 120: 103430.
- [53] BELOUSOV I, LARGE R R, MEFFRE S, DANYUSHEVSKY L V, STEADMAN J, BEARDSMORE T. Pyrite compositions from VHMS and orogenic Au deposits in the Yilgarn Craton, Western Australia: Implications for gold and copper exploration [J]. *Ore Geology Reviews*, 2016, 79: 474–499.
- [54] SUN G T, ZENG Q D, ZHOU L L, WANG Y B, CHEN P W. Trace element contents and in situ sulfur isotope analyses of pyrite in the Baiyun gold deposit, NE China: Implication for the genesis of intrusion-related gold deposits [J]. *Ore Geology Reviews*, 2020, 118: 103330.
- [55] MATHIEU L. Detecting magmatic-derived fluids using pyrite chemistry: Example of the Chibougamau area, Abitibi Subprovince, Québec [J]. *Ore Geology Reviews*, 2019, 114: 103127.
- [56] ZHANG Y, SHAO Y J, CHEN H Y, LIU Z F, LI D F. A hydrothermal origin for the large Xinqiao Cu–S–Fe deposit, Eastern China: Evidence from sulfide geochemistry and sulfur isotopes [J]. *Ore Geology Reviews*, 2017, 88: 534–549.
- [57] SOUTHAM G, SAUNDERS J A. The geomicrobiology of ore deposits [J]. *Economic Geology*, 2005, 100: 1067–1084.
- [58] GREGORY D D, LARGE R R, HALPIN J A, BATURINA E L, LYONS T W, WU S, DANYUSHEVSKY L, SACK P J, CHAPPAZ A, MASLENNIKOV V V, BULL S W. Trace element content of sedimentary pyrite in black shales [J]. *Economic Geology*, 2015, 110: 1389–1410.
- [59] KEITH M, SMITH D J, DOYLE K, HOLWELL D A, JENKIN G R T, BARRY T L, BECKER J, RAMPE J. Pyrite chemistry: A new window into Au–Te ore-forming processes in alkaline epithermal districts, Cripple Creek, Colorado [J]. *Geochimica Et Cosmochimica Acta*, 2020, 274: 172–191.
- [60] SHU Q H, CHANG Z S, MAVROGENES J. Fluid compositions reveal fluid nature, metal deposition mechanisms, and mineralization potential: An example at the Haobugao Zn–Pb skarn, China [J]. *Geology*, 2021, 49: 473–477.
- [61] BARKER S L L, HICKEY K A, CLINE J S, DIPPLE G M, KILBURN M R, VAUGHAN J R, LONGO A A. Uncloaking invisible gold: Use of nanosims to evaluate gold trace elements, and sulfur isotopes in pyrite from carlin-type gold deposits [J]. *Economic Geology*, 2009, 104: 897–904.
- [62] BAUMGARTNER R J, CARUSO S, FIORENTINI M L, VAN KRANENDONK M J, MARTIN L, JEON H, PAGÈS A, WACEY D. Sulfidization of 3.48 billion-year-old stromatolites of the Dresser Formation, Pilbara Craton: Constraints from in-situ sulfur isotope analysis of pyrite [J]. *Chemical Geology*, 2020, 538: 119488.
- [63] BONNETTI C, ZHOU L L, RIEGLER T, BRUGGER J, FAIRCLOUGH M. Large S isotope and trace element fractionations in pyrite of uranium roll front systems result from internally-driven biogeochemical cycle [J]. *Geochimica Et Cosmochimica Acta*, 2020, 282: 113–132.
- [64] DORA M L, UPADHYAY D, RANDIVE K R, SHAREEF M, BASWANI S R, RANJAN S. Trace element geochemistry of magnetite and pyrite and sulfur isotope geochemistry of pyrite and barite from the Thanewasna Cu–(Au) deposit, western Bastar Craton, central India: Implication for ore genesis [J]. *Ore Geology Reviews*, 2020, 117: 103262.
- [65] GREGORY D, MUKHERJEE I, OLSON S L, LARGE R R, DANYUSHEVSKY L V, STEPANOV A S, AVILA J N, CLIFF J, IRELAND T R, RAISWELL R, OLIN P H, MASLENNIKOV V V, LYONS T W. The formation mechanisms of sedimentary pyrite nodules determined by trace element and sulfur isotope microanalysis [J]. *Geochimica Et Cosmochimica Acta*, 2019, 259: 53–68.
- [66] KEITH M, HAASE K M, KLEMD R, KRUMM S, STRAUSS H. Systematic variations of trace element and sulfur isotope compositions in pyrite with stratigraphic depth in the Skouriotissa volcanic-hosted massive sulfide deposit, Troodos ophiolite, Cyprus [J]. *Chemical Geology*, 2016, 423: 7–18.
- [67] OHMOTO H, LASAGA A C. Kinetics of reactions between aqueous sulfates and sulfides in hydrothermal systems [J]. *Geochimica et Cosmochimica Acta*, 1982, 46: 1727–1745.
- [68] OHMOTO H, GOLDBERGER M B. Sulfur and carbon isotopes [M]//Geochemistry of hydrothermal ore deposits. New York: Wiley, 1997: 517–611.
- [69] KAJIWARA Y, KROUSE H R. Sulfur isotope partitioning in metallic sulfide systems [J]. *Canadian Journal of Earth Sciences*, 1971, 8: 1397–1408.

- [70] OHMOTO H. Systematics of sulfur and carbon isotopes in hydrothermal ore deposits [J]. *Economic Geology*, 1972, 67: 551–578.
- [71] TAYLOR H P. The application of oxygen and hydrogen isotope studies to problems of hydrothermal alteration and ore deposition [J]. *Economic Geology*, 1974, 69: 843–883.
- [72] XUAN Y S, YUAN S D, MI J R, ZHAO P L, YUAN Y B, ZHANG D L. Preliminary studies on the fluid inclusions and H–O isotopic geochemistry of the Baoshan copper polymetallic deposit, Hunan Province [J]. *Acta Petrologica Sinica*, 2017, 33: 873–886. (in Chinese)
- [73] JIANG Y H, JIANG S Y, DAI B Z, LIAO S Y, ZHAO K D, LING H F. Middle to late Jurassic felsic and mafic magmatism in southern Hunan province, southeast China: Implications for a continental arc to rifting [J]. *Lithos*, 2009, 107: 185–204.
- [74] SIBSON R H, ROBERT F, POULSEN K H. High-angle reverse faults, fluid-pressure cycling, and mesothermal gold-quartz deposits [J]. *Geology*, 1988, 16: 551.
- [75] WU Y F, LI J W, EVANS K, KOENIG A E, LI Z K, O'BRIEN H, LAHAYE Y, REMPEL K, HU S Y, ZHANG Z P, YU J P. Ore-forming processes of the Daqiao epizonal orogenic gold deposit, west Qinling Orogen, China: Constraints from textures, trace elements, and sulfur isotopes of pyrite and marcasite, and Raman spectroscopy of carbonaceous material [J]. *Economic Geology*, 2018, 113: 1093–1132.
- [76] PATTRICK R A D, DORLING M, POLYA D A. TEM study of indium- and copper-bearing growth-banded sphalerite [J]. *The Canadian Mineralogist*, 1993, 31: 105–117.
- [77] JOHAN Z. Indium and germanium in the structure of sphalerite: An example of coupled substitution with Copper [J]. *Mineralogy and Petrology*, 1988, 39: 211–229.
- [78] ROSE A W. The effect of cuprous chloride complexes in the origin of red-bed copper and related deposits [J]. *Economic Geology*, 1976, 71: 1036–1048.
- [79] DRUMMOND S E, OHMOTO H. Chemical evolution and mineral deposition in boiling hydrothermal systems [J]. *Economic Geology*, 1985, 80: 126–147.
- [80] BENNING L G, SEWARD T M. Hydrosulphide complexing of Au (I) in hydrothermal solutions from 150–400 °C and 500–1500 bar [J]. *Geochimica et Cosmochimica Acta*, 1996, 60: 1849–1871.
- [81] CHINNASAMY S S, MISHRA B. Greenstone metamorphism, hydrothermal alteration, and gold mineralization in the genetic context of the granodiorite-hosted gold deposit at Jonnagiri, Eastern Dharwar Craton, India [J]. *Economic Geology*, 2013, 108: 1015–1036.
- [82] POKROVSKI G S, BORISOVA A Y, BYCHKOV A Y. Speciation and transport of metals and metalloids in geological vapors [M]. *Thermodynamics of Geothermal Fluids*. Berlin, Boston: De Gruyter, 2013: 165–218.
- [83] GAO S, XU H, LI S R, SANTOSH M, ZHANG D S, YANG L J, QUAN S L. Hydrothermal alteration and ore-forming fluids associated with gold-tellurium mineralization in the Dongping gold deposit, China [J]. *Ore Geology Reviews*, 2017, 80: 166–184.
- [84] GRUNDLER P V, BRUGGER J, ETSCHMANN B E, HELM L, LIU W H, SPRY P G, TIAN Y, TESTEMALE D, PRING A. Speciation of aqueous tellurium(IV) in hydrothermal solutions and vapors, and the role of oxidized tellurium species in Te transport and gold deposition [J]. *Geochimica et Cosmochimica Acta*, 2013, 120: 298–325.

宝山 Cu–Pb–Zn 多金属矿床流体演化证据： 来自黄铁矿原位硫同位素和微量元素组成的制约

张俊柯^{1,2}, 邵拥军^{1,2}, 陈可^{1,2}, 谭华杰^{1,2}, 谭睿昶^{1,2}, 张天栋^{1,2}, 刘忠法^{1,2}

1. 中南大学 有色金属成矿预测教育部重点实验室, 长沙 410083;

2. 中南大学 地球科学与信息物理学院, 长沙 410083

摘要: 对宝山铜多金属矿床中的黄铁矿进行原位 LA-ICP-MS 和硫同位素研究, 以探讨矿床的成矿过程和元素富集机制。选取矽卡岩型矿石中的 3 个世代黄铁矿(Py I、Py II 和 Py III)以及中部、西部和北部(C_Py、W_Py 和 N_Py)矿区赋存在碳酸盐岩中的硫化物矿石里的黄铁矿为研究对象进行比较。与 Py I 和 Py III 相比, Py II 中大多数元素的含量明显较高。C_Py 中砷和硒的含量很高且变化范围大, 这两种元素在 C_Py 的生长带中呈解耦趋势。W_Py 和 N_Py 中具有最高的砷、硒和铅含量。这些结果表明, 成矿过程中伴随着温度的剧烈变化以及流体混合作用。岩浆热液间歇脉冲、流体混合作用以及水-岩相互作用导致温度和 $f(\text{O}_2)$ 波动以及变化。黄铁矿的硫同位素暗示硫主要为岩浆来源。 $f(\text{O}_2)$ 条件的变化是导致各类黄铁矿中硫同位素组成轻微差异的主要原因。最后, 提出成矿模式以阐明宝山成矿过程。

关键词: 黄铁矿; 微量元素; 原位硫同位素; 水压致裂; 流体混合

(Edited by Bing YANG)